Subcellular In Vivo ^{1}H MR Spectroscopy of *Xenopus laevis* Oocytes

Seung-Cheol Lee,* Jee-Hyun Cho,* Daniel Mietchen,*†‡ Young-Sook Kim,* Kwan Soo Hong,* Chulhyun Lee,* Dongmin Kang,§ Ki Deok Park,¶ Byong-Seok Choi,‖ and Chaejoon Cheong*

*Division of Proteome Research, Korea Basic Science Institute, Yusung-gu, Daejeon 305-333, Korea; †Fraunhofer Institute for Biomedical Engineering, Department of Magnetic Resonance, Sankt Ingbert, Germany; ‡University of the Saarland, Faculty of Physics and Mechatronics, Saarbrücken, Germany; §Chuncheon Center, Korea Basic Science Institute, Chuncheon, Kangwon-do 200-701, Korea; ¶Gwangju Center, Korea Basic Science Institute, Gwangju 500-757, Korea; and ‖Department of Chemistry and National Creative Research Initiative Center, Korea Advanced Institute of Science and Technology, Yusung-gu, Daejeon 305-701, Korea

ABSTRACT In vivo magnetic resonance (MR) spectra are typically obtained from voxels whose spatial dimensions far exceed those of the cells they contain. This study was designed to evaluate the potential of localized MR spectroscopy to investigate subcellular phenomena. Using a high magnetic field and a home-built microscopy probe with large gradient field strengths, we achieved voxel sizes of (180 μm)^3. In the large oocytes of the frog *Xenopus laevis*, this was small enough to allow the recording of the first compartment-selective in vivo MR spectra from the animal and vegetal cytoplasm as well as the nucleus. The two cytoplasmic regions differed in their lipid contents and NMR lineshape characteristics—differences that are not detectable with whole-cell NMR techniques. In the nucleus, the signal appeared to be dominated by water, whereas other contributions were negligible. We also used localized spectroscopy to monitor the uptake of diminazene acturate, an antitrypanosomal agent, into compartments of a single living oocyte. The resulting spectra from the nucleus and cytoplasm revealed different uptake kinetics for the two components of the drug and demonstrate that MR technology is on the verge of becoming a tool for cell biology.

INTRODUCTION

NMR allows detailed insights into molecular properties of liquids or solids, including, for instance, chemical structures and dynamics (1). Several NMR variants additionally provide spatial information (2,3): Spatial maps of water protons, relaxation properties, diffusion or flow inside an animal or human body can be obtained with magnetic resonance imaging (MRI), and in vivo localized magnetic resonance spectroscopy (MRS) delivers chemical spectra at predefined regions of such samples. The spatial resolution of MRI typically ranges between millimeters and hundreds of microns (4,5), whereas MRS—which generates signal from nonwater protons whose concentrations fall far below those of the water protons used in MRI—requires voxel sizes of tens of millimeters for humans to a few millimeters for smaller animals like rodents (6,7). This is far from the lower micrometer range typical of cellular dimensions. However, Aguayo et al. (8) achieved magnetic resonance (MR) microscopic imaging of a large single cell, the *Xenopus laevis* oocyte whose diameter is ~1.2 mm. Since then, *Xenopus* oocytes and other large single cells like *Aplysia californica* neurons (300 μm in diameter) have been used in numerous quantitative water MRI studies that mapped the apparent diffusion coefficients or spin-spin and spin-lattice relaxation times of intracellular water (9–13). With localized MRS, in contrast, only limited success has been reported on a cellular scale: Posse and Aue (14) reported lipid peaks from 250 μm MR slices of *Xenopus* oocytes, but the peaks were unresolved with respect to the different intracellular contributions. The spectrum of the slice through the nucleus hence contained cytoplasmic signal. Grant et al. (15) recorded an MR spectrum from a (220 μm)^3 voxel within an *A. californica* neuron. Nonetheless, as the voxel barely fit inside the cell, intracellular structures could not be distinguished.

Minard and Wind (16) used chemical shift imaging and reported spectra from multiple voxels positioned in a *Xenopus* globule, a translucent sphere of ~100 μm diameter obtained from a juvenile's ovary. The different voxels, however, delivered indistinguishable spectra. Besides, as these globules have no germinal vesicle and do not stain for DNA, they cannot be considered realistic model cells. Thus, in contrast to subcellular MRI, we are not aware of any report of subcellular MRS.

Intracellular molecules have smaller diffusion coefficients than extracellular molecules because intracellular and compartmental boundaries restrict diffusion. This has been exploited in diffusion-weighted MRS to differentiate between intracellular and extracellular signal contributions of nonwater molecules (17,18). Different intracelluar regions, however, cannot be distinguished this way. Some nuclei, e.g., ^{133}Cs and ^{31}P, exhibit chemical shift differences in different environments which can serve to discriminate between an intra- and extracellular location (19,20). Using ^{31}P chemical shift differences or lineshape analysis of ^{14}N ammonium,

Submitted September 1, 2005, and accepted for publication November 16, 2005.

Seung-Cheol Lee, Jee-Hyun Cho, and Daniel Mietchen contributed equally to this work.

Address reprint requests to Chaejoon Cheong, Korea Basic Science Institute, 52 Eoun-dong, Yusung-gu, Daejeon 305-333, Korea. Tel.: 82-42-865-3431; Fax: 82-42-865-3419; E-mail: cheong@kbsi.re.kr.

Seung-Cheol Lee's present address is Dept. of Radiology, University of Pennsylvania, B6 Blockley Hall, 423 Guardian Dr., Philadelphia, PA 19104.

0006-3495/06/03/1797/07 $2.00

doi: 10.1529/biophysj.105.073502

cytoplasmic and vacuolar regions in maize root tissue could be distinguished (21,22). Neither of these methods, though, is voxel selective, nor do they employ ^{1}H, the dominant nucleus in cellular biochemistry.

To achieve subcellular nonwater ^{1}H MRS, the MR setup has to be highly sensitive, invoking the need for a strong static magnetic field, strong gradients, and micro radio frequency (rf) coils. We have previously reported $(2\ \mu m)^2$ in-plane resolution in ^{1}H MR images of 50 μm thickness from cylindrical plant cells that have a planar diameter of tens of microns (23). But MRS voxels can currently not be that small because the ^{1}H signal from nonwater metabolites naturally is very low and because a reduction in MRS voxel size brings about increasing eddy currents that effectively block the MR signal recording. Because the signal/noise ratio (SNR) in NMR increases inversely proportional to the micro rf coil diameter (16) and since intracellular structures scale with cell size, the dimensions of the rf coil and the biological cell size have to be precisely balanced for optimal subcellular signals.

Thus, we confined our study to a cell system with intracellular compartments larger than the smallest voxel dimension we could realistically obtain. Prophase I-arrested stage VI *X. laevis* oocytes fit this condition. The correspondingly large rf coil means SNR loss with respect to smaller possible rf coil dimensions, but this effect was compensated for by the relatively high magnetic field (14.1 T). This approach was aimed at acquiring compartment-specific spectra of an oocyte and at monitoring drug uptake into its subcellular compartments. The drug we selected is an antitrypanosomal agent: diminazene aceturate (also referred to as berenil), the diminazene component of which is known to strongly bind to nucleic acid duplexes by forming hydrogen bonds (24). Consequently, MR spectra obtained with sufficient SNR from the nucleus can be expected to reflect both the transport into the nucleus and the DNA binding of the drug.

MATERIALS AND METHODS

Voxel selection and gradient fields

In strong magnetic fields, chemical shifts can cause a significant displacement error in MRS (25). Table 1 shows the displacement errors at different rf pulse bandwidths and static magnetic field strengths for the chemical shift span of 5 ppm, the range which covers most of the signals relevant for in vivo ^{1}H MRS. They were calculated by dividing 5 ppm by the chemical shift span corresponding to the specified rf bandwith and the magnetic field. The displacement error increases with magnetic field strength and decreases with rf pulse bandwidth. We thus did our experiments with a much higher rf bandwidth (11 kHz) and a shorter rf pulse (0.5 ms) than usually used in MRI. Even under these conditions, the theoretical displacement error is 27.3% at 14.1 T. The large bandwidth, in turn, requires a large magnetic field gradient. Table 2 shows the required gradient field strengths for the respective voxel size and rf bandwidth. They increase with rf pulse bandwidth and decrease with voxel size. At $(180\ \mu m)^3$, our voxel size, a gradient field strength of 1.5 T/m is required. Our gradient coil capacity allows still higher gradient strengths, but these cause larger eddy currents and possibly also signal distortions in MRS experiments.

TABLE 1 Displacement errors at magnetic field strengths and rf pulse bandwidths

	1.5 T	9.4 T	14.1 T	18.8 T
2.75 kHz (2 ms)*	11.8%	72.9%	109.1%	146.3%
5.5 kHz (1 ms)	5.9%	36.4%	54.5%	73.2%
11 kHz (0.5 ms)	2.9%	18.2%	27.3%	36.6%

*The values in brackets represent the length of the respective sinc3 pulses (Bruker Biospin).

Oocyte preparation

Sexually mature *X. laevis* frogs were purchased from Xenopus I (Dexter, MI). Prophase I-arrested stage VI oocytes surgically harvested from ice-anesthetized females were defolliculated by treatment with 0.2% collagenase (Sigma, type I, St. Louis, MO) in 0.33× MR buffer (33 mM NaCl, 0.6 mM KCl, 0.66 mM $CaCl_2$, 0.33 mM $MgCl_2$, 1.7 mM HEPES, pH 7.4) and stored in OR2 buffer (82.5 mM NaCl, 2.5 mM KCl, 1 mM $CaCl_2$, 1 mM $MgCl_2$, 1 mM Na_2HPO_4, 5 mM HEPES, pH 7.6). For the drug uptake experiments, the oocyte was then immersed in an aqueous solution of 250 mM diminaze aceturate (Sigma) and inserted into the MR tube loaded with the same solution. The relatively high drug concentration resulted in noticeable osmotic swelling (up to 6% in diameter, corresponding to a fractional volume change of ~20%) but did not seem to affect the overall state of the oocytes. All frogs used were healthy, and all experimental procedures involving animals were performed in accordance with the institutional ethical guidelines.

MRI and MRS

A homemade MR microscopy probe with a maximum gradient of 10 T/m (23) has been used on a Bruker DMX 600 spectrometer with microimaging system. The radio frequency coil was prepared by winding six turns of enamel-coated copper wire of 0.5 mm outer diameter (received from Bruker Biospin, Karlsruhe, Germany) around a capillary MR tube of 1.7 mm outer and 1.3 mm inner diameter (Wilmad-LabGlass, Buena, NJ). MR images were acquired using a spin-echo sequence with simultaneous suppression of the lipid peaks between 0 and 3 ppm using three successive sinc3 pulses of 3 ms length and 2070 Hz bandwidth centered at 1.5 ppm. The methine peak at 5.3 ppm, however, could not be reached this way. Lipid suppression has been especially important for selecting regions for localized spectroscopy, since at this high magnetic field strength, the lipid image of the lipid-rich oocyte significantly affects the water image, thus hampering correct voxel positioning. The imaging parameters were as follows: field of view = 2.3 mm, pixel size = 18 μm × 18 μm, slice thickness = 200 μm, matrix (MTX) = 128 × 128, spectral bandwidth (SW) = 25 kHz, repetition time (TR) = 2000 ms, echo time (TE) = 10 ms, number of excitations (NEX) = 8, acquisition time (T_{acq}) = 26 min. For the single voxel spectroscopy, one 90° pulse of 0.5 ms and two 180° pulses of 0.4 ms were applied in a point resolved spectroscopy sequence (PRESS) (26), along with spoiling gradients of 1 ms and 100 mT/m between pulses, which led to a minimum echo time of 6.5 ms. For water suppression, three successive sinc3 pulses of 19 ms were applied along with spoiling gradients of 6 ms and 120 mT/m. To minimize localization errors, an rf bandwidth of 11 kHz was chosen, which required gradients of up to 1.5 T/m for a voxel of 180 μm unit length (cf. Table 1). The acquisition parameters were TR = 2000 ms, SW = 10 kHz, acquisition

TABLE 2 Gradient fields required by rf bandwidth and voxel size

	180 μm	100 μm	50 μm
5.5 kHz (1 ms)	0.75 T/m	1.35 T/m	2.7 T/m
11 kHz (0.5 ms)	1.5 T/m	2.7 T/m	5.4 T/m

size = 4096, NEX = 256, T_{acq} = 8.5 min, exponential filter width = 20 Hz, temperature = 18°C. TE = 8.4 ms was used for (180 μm)^3 voxel spectra, and TE = 6.5 ms for (200 μm)^3 voxel spectra. For lipid T_2 measurements in the cytoplasm, localized spectroscopy with (200 μm)^3 voxels was employed with 10 different echo times in intervals of 4 ms, starting at 6.5 ms. The measurement was repeated on five individual oocytes. For magic angle spinning (MAS) experiments, an indirect detection pulsed field gradient nano H{X} probe (4 mm) was used in a Varian (Palo Alto, CA) UNITY INOVA 500 NMR Spectrometer. Four stage VI oocytes were placed in the 40 μl MAS sample tube with 90% H_2O/10% D_2O, and spun at 2.8 kHz. For acquisition, a simple pulse-and-collect method was used. Water suppression was achieved by a weak presaturation pulse of 2.0 s. A 90° flip angle of 14.3 μs and a repetition time of 2.05 s were employed.

Partition coefficient calculation

The partition coefficients were calculated with the ClogP program (available at http://www.biobyte.com, developed by BioByte, Claremont, CA) for the method of Hansch and Leo (27) and with the help of the KOWWIN program (available at http://www.syrres.com/esc/kowwin.htm, developed by Syracuse Research, Syracuse, NY) for the method of Meylan and Howard (28).

RESULTS

Fig. 1 *A* shows the ^{1}H MR image of a single cell, a stage VI *X. laevis* oocyte arrested in prophase I. It comprises three major compartments—nucleus, animal cytoplasm, and vegetal cytoplasm—which are clearly distinguished by intrinsic MRI contrast arising from the compartment-specific spin-spin relaxation times (T_2) of water, concordant with previously recorded water T_2 maps (12). The three cubes in the image indicate the actual position and width selected for the recording of localized spectra from isotropic voxels of (180 μm)^3 in each compartment. Fig. 1 *B* shows ^{1}H MR spectra obtained from these voxels, exhibiting notable differences: In the nucleus, the nonwater signal was very small, whereas large peaks typical of triglycerides could be observed in the animal and vegetal cytoplasm—they represent methine, the glycerol backbone, methylene, and methyl residues, as indicated in the figure. The MR characteristics in the animal and vegetal cytoplasm also differed from each other: At identical voxel size, the integral of the triglyceride peaks in the vegetal cytoplasm was two to three times the value found in the animal cytoplasm, with the actual ratio varying between individual oocytes. The linewidths of the vegetal peaks were twice those of the animal peaks. To examine the reason for this factor, we compared T_2, the spin-spin relaxation times, of the methylene peak at 1.1 ppm in both compartments. Values of 14 ± 1 ms and 12 ± 0.2 ms were obtained for the animal and vegetal cytoplasm, respectively—well in agreement with previously gathered data (12,29). Our in vivo ^{1}H spectra did not reveal metabolites other than triglycerides. To obtain a more resolved spectrum, we subjected several fresh prophase I-arrested stage VI *Xenopus* oocytes to a MAS experiment. Although subcellular variations could not be determined with this whole-cell technique, it yielded spectra with increased resolution and sensitivity, since dipolar broadening and susceptibility variation within the sample are being reduced (30). The triglyceride peaks were better resolved, and small additional peaks—creatine, choline, and phosphatidylcholine at 2.9–3.2 ppm (30)—could be detected (Fig. 2).

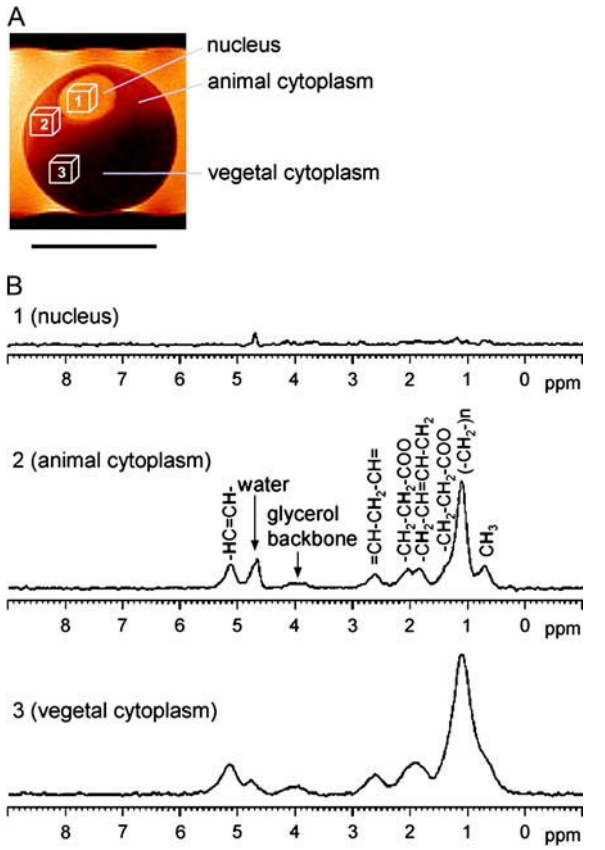

FIGURE 1 In vivo MR spectra from intracellular compartments of a *X. laevis* oocyte. (*A*) High-resolution image of a stage VI (prophase I-arrested) oocyte. Scale bar, 1 mm. Isotropic voxels of (180 μm)^3 were selected for localized spectroscopy of the nucleus as well as the animal and vegetal cytoplasm and are indicated by location and size of the boxes. (*B*) Localized spectra of the voxels indicated in *A*. Tracylglycerol resonances and contributing protons are indicated (assigned after Szczepaniak et al. (51)). Water peak is referenced to 4.7 ppm. Note the absence of bleed over from the strong cytosolic lipid signals into the nucleus.

Taking advantage of the subcellular resolution now achieved with MRS, we examined, upon drug delivery, the spectroscopic changes in the three subcellular compartments of the *Xenopus* oocyte over time. Fig. 3 *A* depicts the chemical structure of diminazene aceturate, with its MR signaling proton sites labeled (*a–e*). Fig. 3 *B* shows an MR spectrum of the medium, together with a spectral time series from the three oocyte compartments. The diminazene peaks (*b* and *c*) appear at 6.7 and 7.1 ppm, and the aceturate peaks (*a*, *d*, and *e*) at 1.8, 3.4, and 7.8 ppm. In the nucleus, diminazene and aceturate peaks showed differing kinetics: The aceturate peaks reached levels equivalent to those in the medium by 1 h after immersion, whereas the diminazene peaks were notably smaller at that time and, after 6 h, reached only half the intensity of those in the medium. In the cytoplasm, the drug

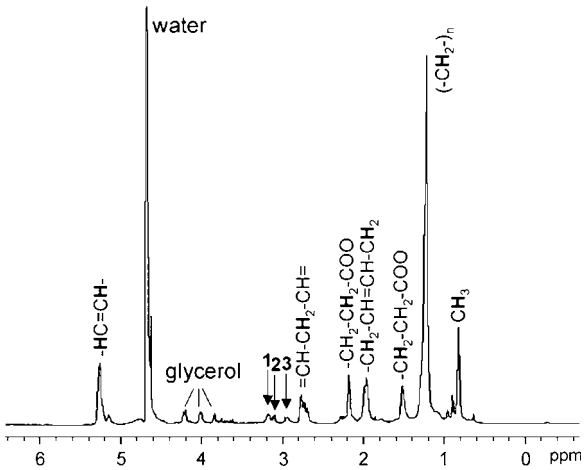

FIGURE 2 ^{1}H MAS MR spectrum of *X. laevis* oocytes. Four oocytes were spun at 2.8 kHz. Arrows indicate phospholipids (28): (*1*) phosphatidylcholine, (*2*) choline, and (*3*) creatine. Water peak is referenced to 4.7 ppm.

signal was superimposed with the natural triglyceride peaks. Diminazene peaks were not observed within 6 h, whereas aceturate peaks slowly grew with time.

DISCUSSION

Subcellular spectroscopy

The negligible lipid signal in the spectrum obtained from the voxel in the nucleus demonstrates that although localization errors are not entirely evitable in high-field MRS, there is no significant signal spillover from the surrounding lipid-rich cytoplasm. Localization errors in our experiments can hence be considered to be confined within each compartment. Besides, the lack of lipid signal in the nucleus is consistent with the lack of yolk platelets in the nucleus (31,32) and with a previous lipid ^{1}H MRI study of the *Xenopus* oocyte (12). The observed differences in the lipid peak integrals in the cytoplasm also affirm earlier studies of yolk distribution within the oocyte (31) and agree well with triglycerides being the major neutral lipid component of many types of cells (33).

The similar T_2 values of the animal and vegetal methylene peaks imply that molecular motion occurs at the same timescale in both compartments and cannot account for the linewidth difference. Instead, the broad linewidth in the vegetal cytoplasm may stem from magnetic inhomogeneity in that region. We conclude that yolk platelets—lipoprotein assemblies of different sizes (34)—have caused the inhomogeneities in the vegetal cytoplasm, perhaps along with mitochondria and other organelles with paramagnetic components. In line with this interpretation, previous studies found an apparent mitochondrial asymmetry along the animal-vegetal axis of the *Xenopus* egg (35,36).

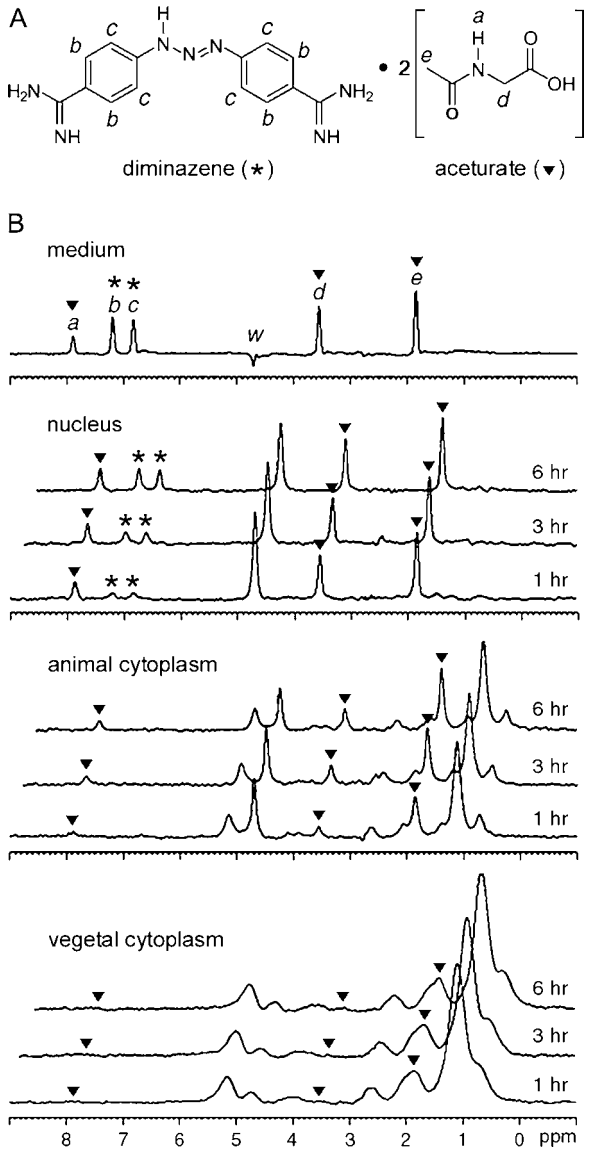

FIGURE 3 Drug uptake into cellular compartments. (*A*) Chemical structure of diminazene aceturate, with MR-visible protons labeled as *a–e*. Diminazene is labeled with an asterisk, and aceturate with inverted solid triangles. (*B*) Localized spectra of the external medium, the nucleus, the animal, and the vegetal cytosolic region of a prophase I-arrested stage VI oocyte in vivo, taken at different times after immersion in diminazene aceturate. Water peak referenced to 4.7 ppm. Intensity scale applies to all spectra. (*a*, *d*, and *e*) Aceturate (▼); (*b* and *c*) diminazene (*). The peak intensities of the diminazene peak *c* at 6.85 ppm and of the aceturate peak *d* at 3.55 ppm have been calculated for each compartment and after 1, 3, or 6 h, as the percentage of the respective peak intensity in the medium: nucleus, 15, 24, and 51 for peak *c* and 81, 84, and 95 for peak *d*; animal, peak *c* not detectable, and 18, 36, and 38 for peak *d*; vegetal, peak *c* not detectable, peak *d* at 1 h not detectable, and 3.2 and 6.2 at 3 h and 6 h, respectively.

The whole-cell MAS spectrum being dominated by lipids is in apparent contrast with previous whole-cell experiments in another large single cell, an *A. californica* neuron (15), which brought about a negligible lipid signal and large amounts of other metabolites, including the neurotransmitter

choline. Considering, though, that the *Aplysia* neuron is an already fully differentiated somatic cell whereas the *Xenopus* oocyte is a germinal cell containing large fat stores to fuel quick embryonic development, these spectroscopically observed differences in lipid contents turn out to simply reflect, in both cases, physiological adaptations to the function of the respective cell type.

Alterations in ^{1}H NMR peak levels from intracellular lipids have been reported in various cell biological processes, such as cell activation, proliferation, and apoptosis (31). Based on our observation that fertilized *X. laevis* oocytes can undergo complete embryogenesis in a NMR tube during in vivo acquisition of MR images (S. C. Lee, D. Mietchen, J.-H. Cho, Y.-S. Kim, C. Kim, K. S. Hong, C. Lee, D. Kang, W. Lee, and C. Cheong, unpublished), applications of localized MRS to the above-mentioned processes would make embryonic development accessible to noninvasive in vivo investigations. Given that early stage *X. laevis* embryos are ~1 mm in diameter, oocytes up to the 8-cell or 16-cell stages would, under optimal conditions, be observable at single-cell resolution with our $(180\ \mu m)^3$ voxel size. In the later stages, the voxels no more provide single cell resolution, but the variation of lipids or other metabolites within a particular region of the developing embryo could still be studied noninvasively and in real time. Alternatively, as the size of *X. laevis* embryos does not change significantly until neurulation (32), a voxel that contains a whole oocyte would allow one to follow total lipid changes during cell division and embryonic development at real time, and the time for localized shimming at each voxel position could be saved.

Drug delivery

The apparent spatial and temporal dissimilarities between diminazene and aceturate signals in the cellular compartments can be explained in terms of membrane permeability and binding strength. The molecular weight of aceturate is 117.1 g/mol and that of diminazene is 281.3 g/mol. Since small molecules cross the cell membrane by passive diffusion at a rate mainly determined by the molecule's hydrophobicity, which is commonly expressed in terms of the partition coefficient P between n-octanol and water (37,38), the permeability of the molecules can be estimated from calculations of the partition coefficients of the drug's components. The method of Hansch and Leo (27) predicts $\log(P)$ to be 0.91 for diminazene and -0.91 for aceturate, which agrees well with the respective values of 1.5 and -1.02 that were obtained following Meylan and Howard (28). These calculations indicate that the membrane is ~2 orders of magnitude more permeable to diminazene than to aceturate. Thus, the low amplitude of the diminazene signal in the nucleus must reflect binding effects. This view is supported by both the signal amplitude and linewidth in the nucleus with time: Depending on the binding strength, bound molecules would give broad NMR peaks or no signal at all, and the diminazene signal is initially (after 1 h) much smaller than that of aceturate but, after 6 h, reaches ~½ of the aceturate amplitude. The linewidth of the diminazene peak in the nucleus is initially about twice as broad as that of aceturate and approaches the latter over time, whereas the linewidths of both molecules in the medium are nearly identical. We interpret these results such that although diminazene penetrates the cell membrane earlier than aceturate due to higher permeability, a large portion of it is strongly bound, and only a small portion of diminazene molecules weakly bound to nuclear macromolecules gives the initial signal. When the binding reaches saturation, nonbound molecules dominate the diminazene signal in the nucleus. The aceturate signal after 1 h being nearly equivalent to that in the medium suggests that aceturate in the nucleus has already approached equilibrium with the medium at that time. The aceturate linewidth in the nucleus does not change, which we attribute to the constant lack of macromolecule binding.

To understand the absence of diminazene signal in both cytoplasmic compartments, macromolecule binding has to be considered once more. The mitochondrial DNA quantity varies with species and cell type, and for a mature *X. laevis* oocyte, it is several hundred times that of nuclear DNA (39). Furthermore, since transcription levels will remain low until the midblastula stage when development speeds up, the cytoplasm is stuffed with high amounts of maternal RNA (40). Finally, proteins—which represent one-third of the oocyte's dry mass, far exceeding the contribution of ribonucleic acids (41)—have been shown to bind large quantities of diminazene in other systems (see Mamman et al. (42) and references therein). So our spectra are consistent with the assumption that all of the cytoplasmic diminazene would have been bound to macromolecules and thus give no MR signal.

The aceturate signal in the animal cytoplasm is much lower than that in the nucleus and increases only slowly. The linewidth, in turn, is broader in the animal cytoplasm than in the nucleus, but remains constant over time. We interpret this such that aceturate experiences faster diffusion in the nucleus than in the macromolecule-rich animal cytoplasm and that, although there is no strong macromolecule-binding of aceturate molecules, they are nonetheless restricted in their translational and rotational motions, which would result in a short spin-spin relaxation time and a correspondingly large linewidth. In the vegetal cytoplasm, the aceturate peaks are still smaller than in the animal cytoplasm, concordant with the vegetal cytoplasm being even more stuffed with maternal macromolecules (31,39,40).

Delivery of drugs across cellular membranes is one of the main goals of current pharmaceutical research (43), including MRI contrast agent development for biological applications (44). It should be noted that the diminazene aceturate concentration we used for the cellular uptake experiment is relatively high (250 mM) but still not even half a percent of the concentration of water which dominates the MR signal. Furthermore, the spectroscopically investigated volume is to

be taken into account—it is just (200 μm)^3 or 8 nl. As the maximum size of a voxel that allows for intracellular spectroscopy in a *Xenopus* oocyte would be about (600 μm)^3, the same SNR as in our experiments could be achieved if the drug concentration were to be reduced by a factor of 27 (i.e., down to ~7 mM). Hence, with reasonable SNR, even one or two millimolar concentrations appear to be detectable noninvasively on a cellular level, rendering localized spectroscopy with *Xenopus* oocytes an attractive methodology to noninvasively determine the permeability of a cell for specific drugs, especially since the membrane of amphibian oocytes frequently serves as a broader membrane model (45–49).

Macromolecular binding, however, prevents an exact quantification of the drug concentration—especially at or near the lower detection limit—in the different cellular compartments, which would be required for a detailed kinetic analysis of drug uptake. Further localized MRS studies probing membrane permeability of drugs should thus seek to calibrate the individual intracellular spectra against data obtained in model membrane systems with known macromolecule concentrations.

As the SNR of NMR experiments increases with magnetic field strength, localized spectroscopy experiments at higher strengths could be promising because they could reduce the minimum detectable drug concentration in the cell. According to the simple $\omega^{7/4}$ law proposed by Hoult (50), a SNR increase by 50% is expected between 14.1 T and 18.8 T. This can lower the detection limit of berenil to submillimolar if a whole cell is selected. The achievable voxel dimension is then mainly limited by the gradient eddy current characteristics—as described above; for an identical voxel size, higher gradients are necessary in a higher magnetic field, inducing larger eddy currents.

CONCLUSION

In vivo localized MR spectra were recorded from subcellular regions within *X. laevis* oocytes. The MR signals in the nucleus, animal, and vegetal cytoplasms were compared at the same voxel size, yielding compartment-specific molecular signatures. Furthermore, the localized spectra revealed different uptake kinetics of an externally applied drug into the individual subcellular compartments. Our experiments demonstrate that in vivo localized MRS allows subcellular distinction in large cells noninvasively, evoking some legitimate hope for future applications to cellular systems of more typical dimensions. The availability of intracellular spectra opens a new window for the investigation of intracellular processes, since the spatial and temporal fingerprints of non-water molecules, be they physiological cellular components or external substances, can directly be followed on a subcellular scale.

We thank P. Callaghan (New Zealand), P. Glover (United Kingdom), and F. Volke (Germany) for critically reading our manuscript, and D. Weisblat (United States) for suggestions and comments in its revision.

This work was supported by the Research-Infra Construction Program and the National Research Laboratory Program (grants to C.C.), by the Center for Biological Modulators of the 21st Century Frontier R&D Program (grant to K.S.H.), and by the National Creative Research Initiative (grant to B.-S.C.) from the Ministry of Science and Technology, Republic of Korea. K.S.H. and C.L. were supported partially by Korean Basic Science Institute projects.

REFERENCES

1. Derome, A. E. 1987. Modern NMR Techniques for Chemistry Research. Pergamon, New York.
2. Gadian, D. G. 1995. NMR and Its Applications to Living Systems. Oxford Science Publications, Oxford.
3. deGraaf, R. A. 1998. In vivo NMR Spectroscopy: Principles and Techniques. John Wiley & Sons, Chichester.
4. Haacke, E. M., R. W. Brown, M. R. Thompson, and R. Venkatesan. 1999. Magnetic Resonance Imaging: Physical Principles and Sequence Design. John Wiley & Sons, New York.
5. Benveniste, H., and S. Blackband. 2002. MR microscopy and high resolution small animal MRI: applications in neuroscience research. *Prog. Neurobiol.* 67:393–420.
6. Barker, P. B., D. O. Hearshen, and M. D. Boska. 2001. Single-voxel proton MRS of the human brain at 1.5T and 3.0T. *Magn. Reson. Med.* 45:765–769.
7. Tkáč, I., P.-G. Henry, P. Andersen, C. D. Keene, W. C. Low, and R. Gruetter. 2004. High resolution in vivo ^{1}H NMR spectroscopy of the mouse brain at 9.4 T. *Magn. Reson. Med.* 52:478–484.
8. Aguayo, J. B., S. J. Blackband, J. Schoeniger, M. A. Mattingly, and M. Hinterman. 1986. Nuclear magnetic resonance imaging of a single cell. *Nature.* 322:190–191.
9. Schoeniger, J. S., N. Aiken, E. Hsu, and S. J. Blackband. 1994. Relaxation time and diffusion NMR microscopy of single neurons. *J. Magn. Reson. B.* 103:261–273.
10. Bowtell, R. W., A. Peters, J. C. Sharp, P. Mansfield, E. W. Hsu, N. Aiken, A. Hosrman, and S. J. Blackband. 1995. NMR microscopy of single neurons using spin-echo and line narrowed 2DFT imaging. *Magn. Reson. Med.* 33:790–794.
11. Hsu, E. W., N. R. Aiken, and S. J. Blackband. 1997. A study of diffusion isotropy in single neurons by using NMR microscopy. *Magn. Reson. Med.* 37:624–627.
12. Sehy, J. V., J. J. Ackerman, and J. J. Neil. 2001. Water and lipid MRI of the *Xenopus* oocyte. *Magn. Reson. Med.* 46:900–906.
13. Sehy, J. V., J. J. Ackerman, and J. J. Neil. 2002. Apparent diffusion of water, ions, and small molecules in the *Xenopus* oocyte is consistent with Brownian displacement. *Magn. Reson. Med.* 48:42–51.
14. Posse, S., and W. P. Aue. 1989. Spectroscopic imaging and gradient-echo microscopy on a single cell. *J. Magn. Reson.* 83:620–625.
15. Grant, S. C., N. R. Aiken, H. D. Plant, S. Gibbs, T. H. Mareci, A. G. Webb, and S. J. Blackband. 2000. NMR spectroscopy of single neurons. *Magn. Reson. Med.* 44:19–22.
16. Minard, K. R., and R. A. Wind. 2002. Picoliter ^{1}H NMR spectroscopy. *J. Magn. Reson.* 154:336–343.
17. van Zijl, P. C., C. T. Moonen, P. Faustino, J. Pekar, J. O. Kaplan, and J. S. Cohen. 1991. Complete separation of intracellular and extracellular information in NMR spectra of perfused cells by diffusion-weighted spectroscopy. *Proc. Natl. Acad. Sci. USA.* 88:3228–3232.
18. Pfeuffer, J., I. Tkáč, and R. Gruetter. 2000. Extracellular-intracellular distribution of glucose and lactate in the rat brain assessed noninvasively by diffusion weighted 1H nuclear magnetic resonance spectroscopy in vivo. *J. Cereb. Blood Flow Metab.* 20:736–746.
19. Wellard, R. M., B. P. Shehan, D. J. Craik, and W. R. Adam. 1994. Factors affecting ^{133}Cs chemical shifts in erythrocytes from cesium-fed rats. *J. Magn. Reson. B.* 104:276–279.

20. McCoy, C. L., C. S. Parkins, D. J. Chaplin, J. R. Griffiths, L. M. Rodrigues, and M. Stubbs. 1995. The effect of blood flow modification on intra- and extracellular pH measured by ^{31}P magnetic resonance spectroscopy in murine tumours. *Br. J. Cancer*. 72:905–911.

21. Lee, R. B., R. G. Ratcliffe, and T. E. Southon. 1990. ^{31}P-NMR measurements of the cytoplasmic and vacuolar P_i content of mature maize roots: relationship with phosphorus status and phosphate fluxes. *J. Exp. Bot.* 41:1063–1078.

22. Lee, R. B., and R. G. Ratcliffe. 1991. Observations on the subcellular distribution of the ammonium ion in maize root tissue using in-vivo ^{14}N-nuclear magnetic resonance spectroscopy. *Planta*. 183:359–367.

23. Lee, S.-C., K. Kim, J. Kim, S. Lee, J. H. Yi, S. W. Kim, K. S. Ha, and C. Cheong. 2001. One micrometer resolution NMR microscopy. *J. Magn. Reson.* 150:207–213.

24. Pilch, D. S., M. A. Kirolos, X. Liu, G. E. Plum, and K. J. Breslauer. 1995. Berenil [1,3-bis(4′-amidinophenyl)triazene] binding to DNA duplexes and to a RNA duplex: evidence for both intercalative and minor groove binding properties. *Biochemistry*. 34:9962–9976.

25. Gruetter, R., G. Adriany, H. Merkle, and P. M. Anderson. 1996. Broadband decoupled, ^{1}H-localized ^{13}C MRS of the human brain at 4 tesla. *Magn. Reson. Med.* 36:659–664.

26. Bottomley, P. A. 1987. Spatial localization in NMR spectroscopy in vivo. *Ann. N. Y. Acad. Sci.* 508:333–348.

27. Hansch, C., and A. J. Leo. 1995. Exploring QSAR: Fundamentals and Applications in Chemistry and Biology. American Chemical Society, Washington, DC.

28. Meylan, W. M., and P. H. Howard. 1995. Atom/fragment contribution method for estimating octanol-water partition coefficients. *J. Pharm. Sci.* 84:83–92.

29. Päuser, S., A. Zschunke, A. Khuen, and K. Keller. 1995. Estimation of water content and water mobility in the nucleus and cytoplasm of *Xenopus laevis* oocytes by NMR microscopy. *Magn. Reson. Imaging* 13:269–276.

30. Weybright, P., K. Mills, N. Campbell, D. G. Cory, and S. Singers. 1998. Gradient, high-resolution, magic angle spinning ^{1}H nuclear magnetic resonance spectroscopy of intact cells. *Magn. Reson. Med.* 39:337–345.

31. Danilchik, M. V., and J. C. Gerhart. 1987. Differentiation of the animal-vegetal axis in *Xenopus laevis* oocytes. I. Polarized intracellular translocation of platelets establishes the yolk gradient. *Dev. Biol.* 122:101–112.

32. Hausen, P., and M. Riebsell. 1991. The Early Development of Xenopus laevis: An Atlas of the Histology. Springer, New York.

33. Hakumäki, J. M., and R. A. Kauppinen. 2000. ^{1}H NMR visible lipids in the life and death of cells. *Trends Biochem. Sci.* 25:357–362.

34. Lee, C.-L., J. Linton, J. S. Soughayer, C. E. Sims, and N. L. Albritton. 1999. Localized measurement of kinase activation in oocytes of *Xenopus laevis*. *Nat. Biotechnol.* 17:759–762.

35. Tourte, M., F. Mignotte, and J. C. Mounolou. 1984. Heterogeneous distribution and replication activity of mitochondria in *Xenopus laevis* oocytes. *Eur. J. Cell Biol.* 34:171–178.

36. Volodina, N., J. M. Denegre, and K. L. Mowry. 2003. Apparent mitochondrial asymmetry in *Xenopus* eggs. *Dev. Dyn.* 226:654–662.

37. Lodish, H., A. Berk, L. S. Zipursky, P. Matsudaira, D. Baltimore, and J. Darnell. 2000. Molecular Cell Biology, 4th ed. Freeman, New York.

38. Sangster, J. 1997. Octanol-Water Partition Coefficients: Fundamentals and Physical Chemistry. John Wiley & Sons, Chichester.

39. Shen, E. L., and D. F. Bogenhagen. 2001. Developmentally regulated packaging of mitochondrial DNA by the HMG-box protein mtTFA during *Xenopus* oogenesis. *Nucleic Acids Res.* 29:2822–2828.

40. Bashirullah, A., R. L. Cooperstock, and H. D. Lipshitz. 1998. RNA localization in development. *Annu. Rev. Biochem.* 67:335–394.

41. Territo, P. R., and A. W. Smits. 1998. Whole-body composition of *Xenopus laevis* larvae: implications for lean body mass during development. *J. Exp. Biol.* 201:1013–1022.

42. Mamman, M., Y. O. Aliu, and A. S. Peregrine. 1993. Comparative pharmacokinetics of diminazene in noninfected Boran (*Bos indicus*) cattle and Boran cattle infected with *Trypanosoma congolense*. *Antimicrob. Agents Chemother.* 37:1050–1055.

43. Orive, G., R. M. Hernandez, A. R. Gascon, A. Dominguez-Gil, and J. L. Pedraz. 2003. Drug delivery in biotechnology: present and future. *Curr. Opin. Biotechnol.* 14:659–664.

44. Allen, M. J., K. W. MacBenaris, P. N. Venkatasubramanian, and T. J. Meade. 2004. Cellular delivery of MRI contrast agents. *Chem. Biol.* 11:301–307.

45. Horowitz, S. B. 1972. The permeability of the amphibian oocyte nucleus, in situ. *J. Cell Biol.* 54:609–625.

46. Horowitz, S. B., and T. W. Pearson. 1981. Intracellular monosaccharide and amino acid concentrations and activities and the mechanism of insulin action. *Mol. Cell. Biol.* 1:769–784.

47. Kusano, K., R. Miledi, and J. Stinnakre. 1977. Acetylcholine receptors in the oocyte membrane. *Nature*. 270:739–741.

48. Dascal, N. 1987. The use of *Xenopus* oocytes for the study of ion channels. *CRC Crit. Rev. Biochem.* 22:317–387.

49. Päuser, S., K. Keller, A. Zschunke, and C. Mügge. 1993. Study of the membrane permeability of a paramagnetic complex on single cells by NMR microscopy. *Magn. Reson. Imaging* 11:419–427.

50. Hoult, D. I., and R. E. Richards. 1976. Signal-to-noise ratio of nuclear magnetic resonance experiment. *J. Magn. Reson.* 24:71–85.

51. Szczepaniak, L. S., E. E. Babcock, F. Schick, R. L. Dobbins, A. Garg, D. K. Burns, J. D. McGarry, and D. T. Stein. 1999. Measurement of intracellular triglyceride stores by ^{1}H spectroscopy: validation in vivo. *Am. J. Physiol.* 276:E977–E989.